npj | Quantum Materials

www.nature.com/npjquantmats

ARTICLE OPEN

Check for updates

Tracking photocarrier-enhanced electron-phonon coupling in nonequilibrium

Shi-Qi Hu[1,2,4], Hui Zhao[1,2,4], Chao Lian[1], Xin-Bao Liu[1,2], Meng-Xue Guan[1,2] and Sheng Meng[1,2,3]✉

Light-modulated electron-phonon coupling (EPC) is significant in many intriguing phenomena including light-enhanced superconductivity, polaron formation, and hidden charge orders, which provides a powerful strategy to engineer materials' functionalities on demand. Here we explore EPC in photoexcited graphene during the ultrafast photocarrier dynamics with a phonon bath. Via analysing energy transport between electrons and phonons, light-induced EPC enhancement by more than one order of magnitude is demonstrated, which originates from the dynamic distribution of photoexcited carriers out of equilibrium. Excellent agreements between theory and experiment have been achieved, justifying the validity of the present approach for extracting excited-state dynamic properties. Our result unravels a crucial impact of photoexcitation on EPC by modulating the density and distribution of photocarriers, and provides a useful strategy for tracking ultrafast EPC in real time.

npj Quantum Materials (2022)7:14; https://doi.org/10.1038/s41535-021-00421-7

INTRODUCTION

Electron-phonon coupling (EPC) is one of the fundamental topics in condensed matter physics and is highly relevant to many intriguing phenomena[1] such as the conventional superconductivity[2], phonon-assisted optical absorption[3,4], and formation of charge density waves[5,6]. The EPC properties of materials play an important role in both fundamental physics and realistic applications such as power transmission[7–10], carrier transport[11,12] and solar cells[13–16]. With the rapid development on femtosecond laser technologies, light-modulated EPC attracts extensive attentions recently. Pomarico et al.[17] and Sentef et al.[18] suggested that the EPC in graphene can be strengthened by light due to the presence of distorted lattice and phonon nonlinearity. The possibility of light-induced superconductivity in cuprates[19–21] and molecular solids[22,23] was investigated via coherent optical control of lattice vibrations[17,21,24]. Moreover, laser-excited surface plasmon is demonstrated as a rational way to enhance the EPC in metallic crystals[25]. These studies reveal advantages of photoexcitation to control quantum properties in nonequilibrium phases and might inspire the ways to engineer materials' functionalities on demand.

In general, light modulation of EPC requires effective light-matter and electron-phonon (e-ph) interactions. Due to the complex interactions and excitation dynamics beyond the ground state, the characterization and mechanism of the light-modulated EPC are not fully understood. The impact of photoexcitation on EPC and its time evolutions are still elusive, since in literature the EPC was often treated in a static picture even when ultrafast photoexcitation is present[26,27]. Thanks to its band structure, graphene represents a superior candidate for the study of light-modulated EPC dynamics[28]. The gapless Dirac cone not only gives rise to the broadband and ultrafast optical responses[29–31], but also provides resonant EPC channels between Dirac fermions and phonons. The linear dispersion of Dirac cone guarantees an ineffective electrostatic screening[32–36], which benefits the EPC enhancement[37,38]. Another advantage of graphene is that abundant carrier dynamic processes such as ultrafast carrier cooling[39–42] and carrier multiplication[43–47] offer a good platform for studying nonequilibrium EPC by e-ph scatterings[48–53], where the state of carriers is expected to have an impact on EPC properties[26,54,55].

Here we study the nonequilibrium EPC in photoexcited graphene with the help of newly developed real-time time-dependent density-functional theory (rt-TDDFT) schemes[56–59]. We find a strong light-induced EPC enhancement by monitoring the EPC strength λ and matrix $\langle g_f^2 \rangle_F$ during ultrafast photocarrier relaxation. The good agreements between the EPC strength extracted here and the data fitted to experimental Raman spectroscopy proves the validity of the present dynamic approach for extracting excited-state properties. Different from existing models which rely on coherent lattice vibrations and distortions[17,18], light-enhanced EPC identified here demonstrates that the photoexcited carriers, whose nonequilibrium distribution offers additional channels for e-ph scatterings, are crucial for modulating EPC on demand. Our results suggest a way towards dynamic optical control of EPC and related quantum phenomena, such as superconductivity[19–24], polaron formation[60,61], charge density waves[5,6] and quantum Hall effects[50,62–64].

RESULTS AND DISCUSSION

Carrier and phonon dynamics

After laser illumination, the photocarriers are produced in the Dirac bands by generation of photoexcited electron-hole (e-h) pairs (Fig. 1b). Within hundreds of femtoseconds, the photocarriers cool down through the energy and momentum redistribution, where the e-ph interaction plays an important role[39,42,45,48,49,52]. Because of the e-h symmetry, the relaxation process is illustrated only by the population of electronic photocarriers $n(t)$ in Fig. 1c, $n(t) = \int_{E\ \text{in}\ \pi^*\ \text{bands}} n_e(E - E_f, t)\, dE$, where $n_e(E - E_f, t)$ is the energy distribution of excited electron carriers (EECs) on π^* bansd and E_f is the Fermi level. Since the n

[1]Beijing National Laboratory for Condensed Matter Physics and Institute of Physics, Chinese Academy of Sciences, Beijing 100190, P. R. China. [2]School of Physical Sciences, University of Chinese Academy of Sciences, Beijing 100049, P. R. China. [3]Songshan Lake Materials Laboratory, Dongguan, Guangdong 523808, China. [4]These authors contributed equally: Shi-Qi Hu and Hui Zhao. ✉email: smeng@iphy.ac.cn

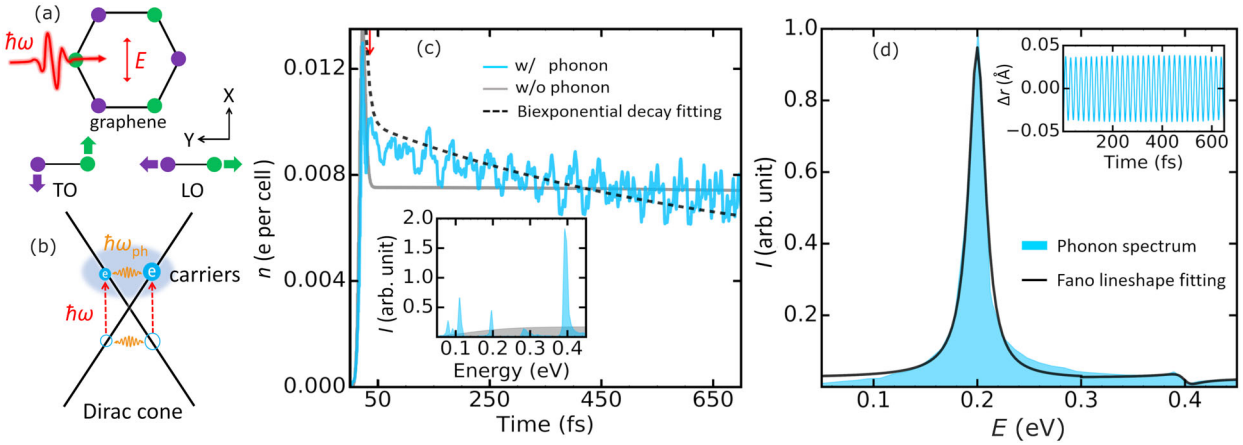

Fig. 1 Carrier and phonon dynamics in photoexcited graphene. a Schematic illustration showing laser illumination and the E_{2g} phonon@**Γ** mode in graphene lattice. Red arrow shows the polarization direction of laser. **b** Illustration of photoexcitation process (red dash arrows) and EPC (orange spring arrows) in graphene. The filled and empty blue circles label photoexcited electrons and holes respectively. **c** Photocarrier population $n(t)$ on the π^* band as a function of time with (blue curve) and without (grey curve) phonons. The dashed black line is the fitting with a biexponential decay. The red arrow labels the end of the pulse (t ~30 fs). The inset shows the Fourier analysis on $n(t)$ with (blue shade) and without (grey shade) phonons. **d** The phonon spectrum (blue shade). The solid black line is fitting to the Fano lineshape. The inset shows the oscillation of carbon atom displacement.

here is proportional to the electron temperature T_e (Supplementary Note 8 and Supplementary Fig. 3), the evolution of $n(t)$ is equivalent to the change of T_e in describing the carrier relaxation.

In the absence of phonons (i.e., clamped ions), the carrier population after photoexcitation ($t > 30$ fs) remains almost unchanged over time due to the lack of decay channels. In contrast, in the presence of phonons, $n(t)$ shows a biexponential decay, which includes two distinct time constants τ_1~7 fs and τ_2~650 fs. The τ_1 corresponds to the full width at half maximum (FWHM) of laser pulse and implies a rapid recombination of e-h pairs after photoexcitation. While τ_2 represents the relaxation time of residual hot carriers interacting with optical phonons. The τ_2 obtained from our simulations agrees well with that extracted from experimental measurements (100 fs–1 ps)[39,42,48,65]. In the presence of phonons, $n(t)$ presents a phonon-resonant oscillation along with its decaying behaviour. As shown in the inset of Fig. 1c, the Fourier analysis of population $n(t)$ contains the E_{2g} phonon@**Γ** frequency (0.2 eV) and its doubling (0.4 eV). The comparison of photocarrier evolution with and without phonons confirms the EPC effect, which provides significant cooling channels for photocarrier relaxation.

During the photocarrier relaxation, the EPC leads to asymmetric phonon peaks in the simulated Raman spectrum (Fig. 1d) through Fano resonance[53,66,67]. The cross term of the e-ph scattering amplitudes gives the Fano interference and affects the spectrum configuration, which is also observed in the Raman spectroscopy of Weyl semimetals[68,69]. The asymmetry is proportional to the EPC strength and quantified by the value of Fano factor $|q|$, obtained by fitting the spectrum with the lineshape $A(E) \sim (q+\varepsilon)^2/[\gamma(q^2+1)(1+\varepsilon^2)]$. Here $\varepsilon = 2(E-\hbar\omega_{ph})/\gamma$, $\hbar\omega_{ph}$ and γ are the phonon energy and peak width, respectively. In Fig. 1d, both the harmonic (0.2 eV) and anharmonic (0.4 eV) peaks of E_{2g} phonons@**Γ**[70–72] show the obvious asymmetry with the Fano factor $|q_{harmonic}|$ ~0.04 and $|q_{anharmonic}|$ ~1.3, respectively, implying a strong EPC effect in photoexcited graphene. More phonon dynamic information can be found in Supplementary Note 10.

Light-enhanced EPC

The strong EPC effects introduce a measurable energy transport between the photocarriers and phonons[7,9], characterized by the energy transport rate $P(t) = \Sigma_{k,i}\, \partial E_{k,i}(t)/\partial t$. Here k and i are the $\boldsymbol{k}$ point and band index, respectively; $E_{k,i}(t) = n_{k,i}(t)\varepsilon_{k,i}(t)$ is the carrier energy on the ith band at wavevector $\boldsymbol{k}$ in the Brillouin zone, where $\varepsilon_{k,i}(t)$ is the Kohn-Sham energy level and $n_{k,i}(t)$ is the population of carriers. With a ~300 K lattice temperature, the time average of the rate amplitude $P = \langle P(t)\rangle_t$ at t ~50 fs is estimated with and without the laser illumination. The results are plotted as a function of doping concentration in Fig. 2.

The energy transport at the ground state is also investigated for comparison, in the same way, but without laser illumination. The value of ground state P in undoped case is consistent with the experimental measurement by Freitag et al.[10,50]. The doping concentration is tuned by adding electrons/holes and described by the Fermi level shift $\pm(E_f - E_D)$ (Fig. 2a–e). Here E_f is the Fermi level and E_D is the energy level of Dirac point. For undoped case, $E_f = E_D$. The + (−) sign labels the increasing (decreasing) of electron concentration. Similar to the anomalous phonon softening phenomenon[36,73–82], P first increases and then decreases with the increase of doping concentration. It exhibites a logarithmic singularity when the Fermi level shift reaches the half of phonon frequency $\hbar\omega_{ph}$, i.e., $|E_f - E_D| \approx 0.1$ eV.

Figure 2a–e illustrates the electronic origin of this anomaly. The doping concentration affects the energy transport process and renormalizes the phonon energy by adjusting the e-h excitation as well as their couplings with phonons. Due to the zero band gap of Dirac cone, e-h carriers can be vertically excited by optical phonons, if their excitation energy $E_{e\text{-}h}$ is close to the phonon energy $\hbar\omega_{ph}$ and higher than the twice of the Fermi level shift ($E_{e\text{-}h} \approx \hbar\omega_{ph} > 2|E_f - E_D|$). This phonon-induced excitation enables the electrons to respond immediately to the change of phonons, which provides screening and enhances the EPC resonance. The EPC resonance contributes to phonon softening and benefits the energy transport between carriers and phonons. However, when the increase of doping concentration makes the Fermi level shift greater than the half of phonon energy ($2|E_f - E_D| > \hbar\omega_{ph}$), the phonon-induced excitation is switched off due to restrictions of Pauli blocking. The e-h carriers can hardly participate in the EPC-induced energy transport, and the states below the Fermi level can no longer contribute to the screening. For this reason, the doping concentration dependence of P, as well as phonon softening, shows the opposite trendency before and after $2|E_f - ED| = \hbar\omega_{ph}$.

In contrast, under a ~4 μJ · cm^{-2} laser illumination, the excited carrier has an effective electron temperature ~2500 K. The logarithmic singularity of P is completely washed out, because

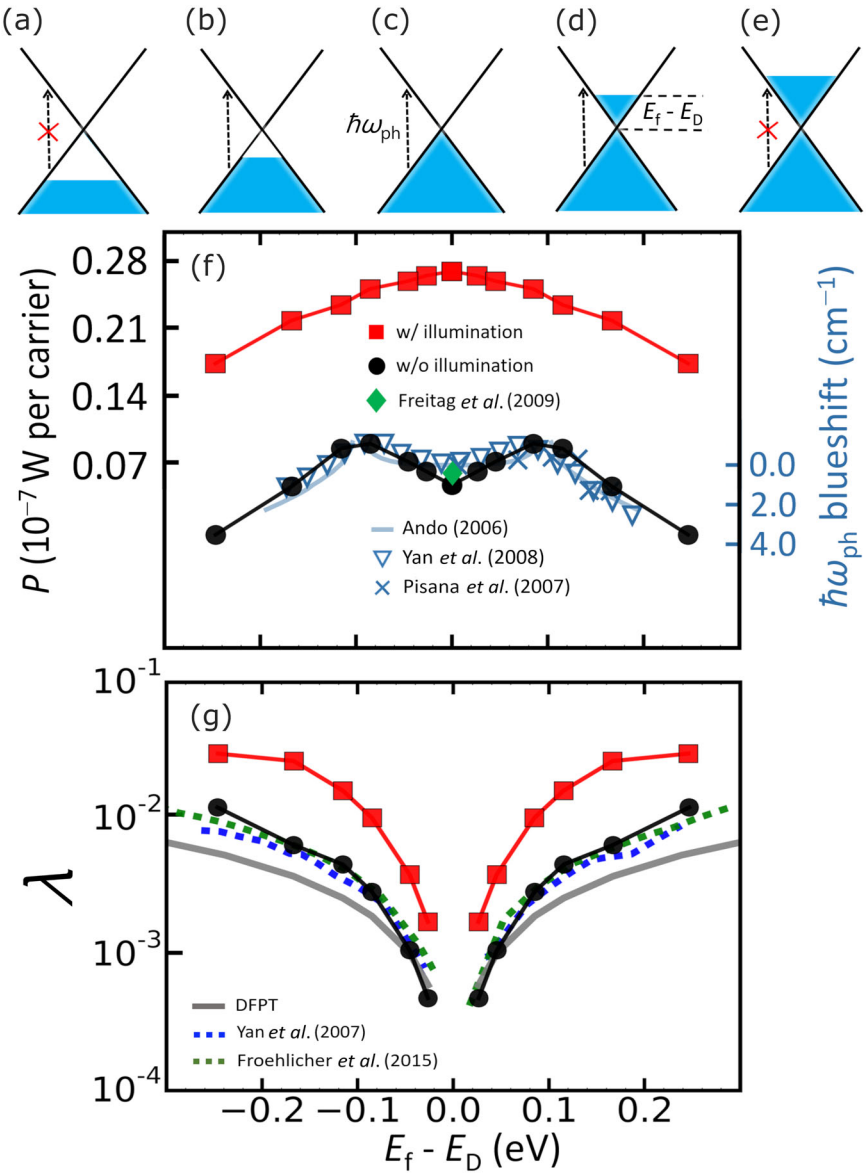

Fig. 2 The energy transport and EPC strength λ in graphene. a–e Schematics showing vertical interband transitions in the Dirac cone with different doping concentrations (represented by $\pm(E_f - E_D)$ where E_f is the Fermi level and E_D is the energy level of Dirac point). Regions with blue shades are filled with electrons. The black arrows indicate the e-h excitations. **f** The energy transport rate P as a function of $E_f - E_D$ with and without laser illumination. The green diamond marks the experimental data of P from Freitag et al.[10]. The blue symbols and lines show anomalous phonon softening measured by Raman spectroscopy in ref. [36], ref. [74] and ref. [81]. **g** The EPC strength λ as a function of $E_f - E_D$ with and without laser illumination. The dashed blue and green lines represent experimental results from ref. [75] and ref. [82].

of the Fermi level broadening introduced by photoexcitation[74]. More importantly, the magnitude of P in the excited state is highly enhanced, implying EPC effect is significantly promoted by photoexcitation.

The different energy transport rate P indicates different EPC strength with and without photoexcitation. Tse et al. derived a generic expression for the EPC-mediated energy transport in graphene using Green function theory[9,83,84], which implies that one can extract the microscopic EPC strength λ directly from the macroscopic energy transport rate P (Supplementary Note 2):

$$\lambda = aP/(n_f N_B), \quad (1)$$

where $a = 12\hbar|E_f - E_D|E_f^2/(\hbar\omega_{ph})^5$, the Fermi level $E_f = \mathrm{sgn}(n)\hbar v_f(\pi|n|)^{1/2}$. The v_f and n are the Fermi velocity and carrier density, respectively. The $N_B = Mu^2\omega_{ph}^2/2\hbar\omega_{ph}$ is the number of phonons, M and u are the mass and displacement of the carbon atom. The $n_f = 1/[\exp(|E_f - E_D|/k_BT)+1]$ is the Fermi-Dirac (F-D) distribution at the energy $|E_f - E_D|$ and temperature T. The same Fermi level E_f is used here to extract the EPC strength λ in the ground and excited state. The ground state λ in the absence of laser illumination is calculated for benchmarking the validity of this approach. Similar to the effective mass picture in band theory, the effects of photoexcitation are naturally included in the difference of effective λ between the ground state and excited states[81].

In Fig. 2g, the EPC strength λ is obtained from the time average of energy transport rate P by Eq. (1) and plotted as a function of doping concentration represented by $E_f - E_D$. Owing to the increasing screening, λ is proportional to the doping concentration. Without laser excitation, the system is near the ground state, thus the doping concentration dependence of λ is consistent with that calculated by the density-functional perturbation theory (DFPT) (See details in Supplementary Note 1).

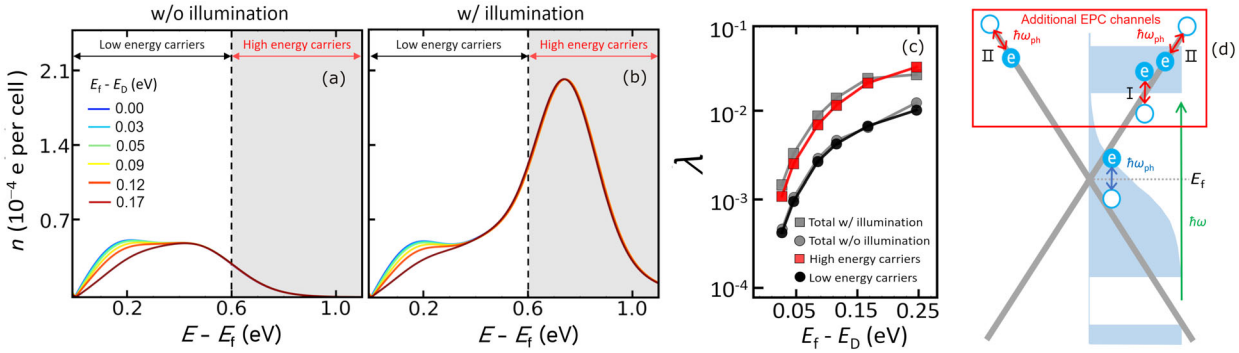

Fig. 3 Carrier resolved EPC in graphene. The energy distribution of EECs on π* band, $n_e(E-E_f)$, without (**a**) and with (**b**) laser illumination at different doping concentrations represented by $E_f - E_D$. The low (high) energy carriers are excited by phonons (photons), which are labelled by black (red) arrows. **c** The λ contributed by low and high energy carriers as a function of doping concentration. **d** Schematic illustration showing the EPC channels in photoexcitation state. Regions with light blue shades are filled with electrons. The deep blue arrow shows the phonon-assisted interband transitions. Without illumination, electrons have the interband transitions by interacting with the phonons, which provide the conventional EPC channels. The green arrow shows the photoexcitation. The red rectangle and red arrows label the additional EPC channels originate from the phonon-assisted intraband transitions (PAITs) of carriers out of equilibrium, which include the electronic broadening effects (process I) and scattering between different ***k*** points (process II).

The deviation at high $|E_f - E_D|$ may be due to the lack of non-adiabatic effects in DFPT, which plays a key role in EPC at high doping levels. Indeed, our results including the non-adiabatic effects show a better agreement with the experiments (Supplementary Note 3)[75,82].

By fitting the relationship between λ and the Fermi level shift $|E_f - E_D|$, the effective EPC matrix of E_{2g} phonon@**Γ** in graphene $\langle g_\Gamma^2 \rangle_F$ can be obtained according to the Eliashberg theory[83,84] (Supplementary Note 1):

$$\lambda = 2\langle g_\Gamma^2 \rangle_F N_F / \hbar\omega_{ph}, \quad (2)$$

where $\langle g_\Gamma^2 \rangle_F = \Sigma^{\pi^*}_{i,j} |g_{ikjk}|^2/4$ is the square sum of EPC matrix elements over the two degenerate π* bands and g_{ikjk} is the electron-phonon matrix element[80,85]. The $N_F(E_f - E_D) = A|E_f - E_D|/\pi(\hbar v_f)^2$ is the density of state (DOS) per spin component of Dirac cone around Fermi level, and A and v_f are the unit-cell area and Fermi velocity, respectively. The ground-state $\langle g_\Gamma^2 \rangle_F$ is evaluated as $\langle g_\Gamma^2 \rangle_F$ = 0.05 eV², which is consistent with the DFPT result $\langle g_\Gamma^2 \rangle_F$ ~0.04[36,80,85] and the experimental values $\langle g_\Gamma^2 \rangle_F$ = 0.043 eV² in ref. [75] and 0.047 eV² in ref. [80] (Supplementary Note 3).

Under laser illumination, the excited-state EPC is dynamic. The effective λ averaged at *t*~50 fs after photoexcitation is shown in Fig. 2g. The λ shows a similar doping dependence with that in the ground state, while its magnitude is significantly enhanced by ~3 times. The fitted $\langle g_\Gamma^2 \rangle_F$ in excited state is ~0.15 eV². The threefold increase of $\langle g_\Gamma^2 \rangle_F$ agrees well with the experimental measurement by time- and angle-resolved photoemission spectroscopy (tr-ARPES)[17], demonstrating that the EPC strength is significantly enhanced by laser excitation, which is different from the continuous wave case (Supplementary Note 7).

In order to gain insights into the mechanism of light-induced EPC enhancement, the population distribution of excited carriers and their contribution to λ are investigated at different doping concentrations (represented by $E_f - E_D$). Note that with charge doping, the total carrier distribution on π* band $n_t(E-E_f)$ includes two parts, $n_t(E-E_f) = n_d(E-E_f) + n_e(E-E_f)$. The $n_d(E-E_f)$ represents the static charge doping, which is proportional to the Fermi level shift $|E_f - E_D|$, and independent of photoexcitation. While $n_e(E-E_f)$ is contributed by the EECs. The distribution of EECs averaged at *t* ~50 fs after photoexcitation is shown in Fig. 3, the EECs now are in the nonequilibrium state. The results are similar on π band with hole doping, because of the e-h symmetry. For both cases, the population of excited carriers decreases with the doping level due to Pauli blocking.

Without laser illumination, $n_e(E-E_f)$ is contributed by the excitation of optical phonons thanks to the gapless Dirac bands, as discussed in Fig. 2a. It is located in the low energy region ($E - E_f < 0.6$ eV) and forms a thermal F-D distribution. In contrast, under laser illumination, the $n_e(E-E_f)$ averaged at *t* ~50 fs is mainly contributed by the photoexcitation and has the none-quilibrium distribution. The nonthermal $n_e(E-E_f)$ mainly occupies high energy levels around $E - E_f = 0.8$ eV, which corresponds to the half of the photon energy $\hbar\omega \approx 1.55$ eV due to the e-h symmetry of Dirac cone. The different energy distribution enables us to divide the excited carriers into low and high energy regions according to their excitation source, the low (high) energy carriers are excited by phonons (photons), which are labelled by black (red) arrows in Fig. 3a, b.

The contribution of EECs to λ at different energy ranges is shown in Fig. 3c. It is clear that the carriers excited by photons (high energy range) and phonons (low energy range) have the dominant contributions to λ in cases with and without laser illumination, respectively. Similar results can also be seen from the photocarrier distribution averaged at *t* ~ 50 fs and the effective EPC matrix elements $\langle g_\Gamma^2 \rangle_F$ as a function of pump fluence J_L, FWHM and wavelength λ_L in Fig. 4. Under different laser conditions, the EPC strength is proportional to the distribution of photocarriers (Supplementary Note 9). The energy-resolved λ and distribution dependence of $\langle g_\Gamma^2 \rangle_F$ confirm that the light-induced EPC enhancement is dominated by the photocarriers, whose nonthermal distribution plays a significant role.

The mechanism for the light-induced EPC enhancement can be understood as schematically shown in Fig. 3d. Upon photoexcitation, nonequilibrium photocarriers generated at the high energy levels have wider distribution due to the large density of state (DOS). The broadening distribution enhances the phonon-assisted intraband transitions (PAITs, as shown in the red rectangle in Fig. 3d), which provide the additional e-ph interaction channels and improve the EPC. The PAITs are induced by the electronic broadening effects[86] (process I) and scattering between different ***k*** points (process II). As shown in Supplementary Fig. 2, the PAITs (blue and black lines in Supplementary Fig. 2) contribute ~80% of the EPC channels, demonstrating a dominant role of PAITs of nonequilibrium photocarriers on EPC enhancement.

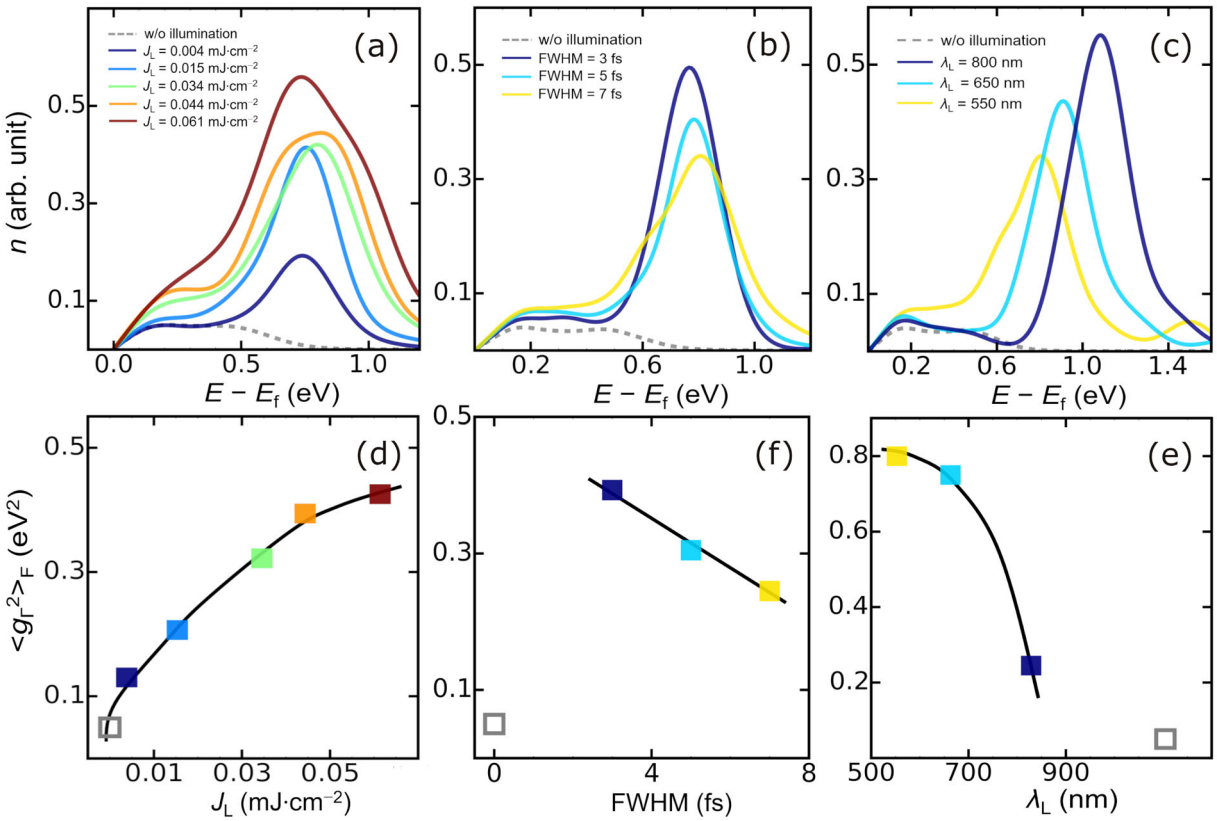

Fig. 4 The carrier distribution and EPC under different conditions. The photoexcited carrier distribution on π* band under (**a**) different pump fluence J_L (λ_L = 800 nm, FWHM ~7 fs), (**b**) FWHM (λ_L = 800 nm, J_L ~ 0.035 mJ/cm^2), and (**c**) wavelength λ_L (FWHM ~7 fs, J_L ~0.035 mJ/cm^2) in undoped graphene. The effective EPC matrix elements $\langle g_\Gamma^2 \rangle_F$ as a function of (**d**) pump fluence, (**e**) FWHM and (**f**) wavelength. The grey open marks label the physical quantities without laser illumination. The black solid line is guide to eyes.

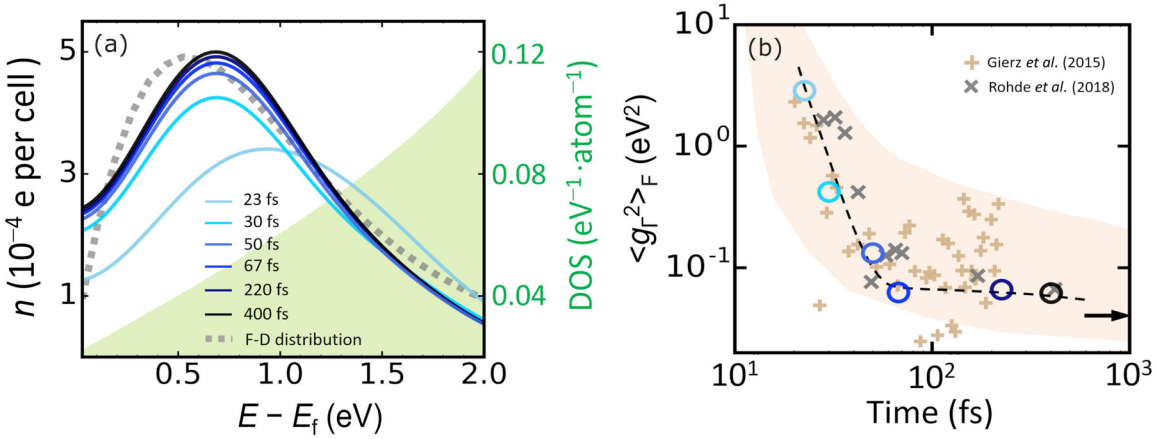

Fig. 5 Tracking the ultrafast EPC in real time. a The energy distribution of different EECs states in the undoped graphene where the Fermi level locates at the Dirac point i.e., $E_f = E_D$. The grey dashed line labels the Fermi-Dirac distribution at T_e = 5000 K. The yellow green shade shows the electronic density of states (DOS). **b** The effective $\langle g_\Gamma^2 \rangle_F$ as a function of time. The tan and grey crosses label the effective $\langle g_\Gamma^2 \rangle_F$ extracted from dynamic carrier states measured experimentally in ref. [44] and ref. [42]. The tan shadow and black dashed line are guides to eyes. The arrow labels the value of $\langle g_\Gamma^2 \rangle_F$ in equilibrium where $\langle g_\Gamma^2 \rangle_F$ ~0.05 eV^2.

Real-time tracking on the light-enhanced EPC dynamics

To further illustrate the impact of photocarrier distribution on EPC dynamics, we choose to study the undoped graphene under a laser fluence of ~44 μJ · cm^{-2} and analyse the ultrafast EPC during photocarrier relaxation. Figure 5a shows the distribution of EECs at different time $n_e(E - E_f, t)$. For comparison, the F-D distribution with an electron temperature T_e ~5000 K is marked by grey dash line. As time goes on, the peak of excited-carrier distribution moves from the high energy region to the low energy region and finally approaches the F-D distribution, beaconing the cooling down process of hot carriers.

The corresponding time evolution of effective EPC matrix element $\langle g_\Gamma^2 \rangle_F$ is shown in Fig. 5b (Also in Supplementary Fig. 1 for doping case). With photoexcitation ($t \leq 30$ fs), the carriers are

excited to high energy levels $E - E_f$ ~1.0 eV. The wider distribution of the nonthermal photocarriers in energy and momentum space provides additional channels for e-ph interactions which enable stronger EPC. The $\langle g_f^2 \rangle_F$ is significantly enhanced by 2~3 orders of magnitude ($\langle g_f^2 \rangle_F > 1$ eV^2). After the pulse duration ($t > 30$ fs), the photocarriers relax towards equilibrium, the energy and momentum range of carrier distribution is suppressed and thus the EPC channels become limited. The light-enhanced $\langle g_f^2 \rangle_F$ decreases again over time. Comparing to experiment, we successfully rebuild the time evolution of EPC strength using Eqs. (1) and (2), the only required input is the data of carrier states (i.e., population and energy distribution of carriers) from tr-ARPES measurements[42,44]. Our theoretical results show a good agreement with effective $\langle g_f^2 \rangle_F$ extracted from experiments (Supplementary Note 4), demonstrating the effectiveness of the strategy for tracking ultrafast EPC. The value of $\langle g_f^2 \rangle_F$ is expected to converge to the equilibrium value ($\langle g_f^2 \rangle_F$ ~0.05 eV^2) within a picosecond timescale as the hot carriers cool down to equilibrium.

The dynamic $\langle g_f^2 \rangle_F$ implies that ultrafast EPC in the excited state is dependent on the photocarrier distribution, which enables not only the real time measurement, but also precise manipulation of EPC by optical technologies. Direct evaluation of EPC strength has been recently achieved in ultrafast spectroscopy experiments[26,27]. The optical modulation can be achieved by coherent control of photocarrier dynamics. For example, the EPC enhancement is expected to be more significant by suppressing other carrier relaxation channels such as electron-electron scattering. The similar analysis may also be used to observe and manipulate the microscopic motions of Cooper pair generation[87,88], superconducting gap fluctuation[89,90] and quantum phase transitions[91].

Our study offers a dynamic analysis on evaluating and tracking nonequilibrium EPC in excited states. The nonequilibrium distribution of photocarriers has a vital impact on the light-enhanced EPC, which provides channels for e-ph scatterings. We believe that such effects are general and measurable in other quantum materials including 2D/3D Dirac or Weyl semimetals, transition metal dichalcogenides[68,86,92–94], and even the conventional metals[95], as long as the wide distribution and the phonon-assisted transitions are available for nonequilibrium photocarriers. More interestingly, since the EPC is connected to multifarious photocarrier dynamics, the topological property of photocarriers such as chiral selection and valley polarization[96–98] may bring some physics and technology applications of light-modulated EPC.

METHODS

TDDFT calculations

The calculations are performed using the time-dependent ab initio package (TDAP) as implemented in SIESTA[99], which has been developed lately to successfully describe photoexcitation dynamics in solids[5,100,101]. In our simulations, numerical atomic orbitals with double zeta polarization are used as the basis set. The $\boldsymbol{k}$ sampling in the Brillouin zone is Gamma-centred $144 \times 144 \times 1$ mesh. The electron-nuclear interactions are described by norm-conserving pseudopotentials with an energy cutoff of 200 Ry in the local-density approximation. For the laser parameters, a Gaussian laser pulse $F = F_0 \cos(\omega t) \exp[-(t - t_0)^2/2\sigma^2]$ with a wavelength of 800 nm ($\hbar\omega \approx 1.55$ eV) is adopted. The polarization is along the zigzag direction (defined as x direction in Fig. 1a). The pulse peak is located at $t_0 = 20$ fs, and the full width at half maximum (FWHM) σ is 7 fs. For phonon dynamics, the coherent E_{2g} phonon@Γ ($\hbar\omega_{ph} \approx 0.2$ eV), as the most dominant optical phonon in graphene[70,102], is considered via introducing an initial weak stretch of the carbon-carbon bond[55] (by 1~2% of the equilibrium bond length). More details about the algorithm and parameters can be found in ref. [103–105].

DATA AVAILABILITY

The data that support the findings of this study are available from the corresponding author upon reasonable request.

CODE AVAILABILITY

The codes used to carry out the DFT calculations used in this work are available from the corresponding authors upon reasonable request.

Received: 12 August 2021; Accepted: 23 December 2021;
Published online: 25 January 2022

REFERENCES

1. Froehlicher, G. Electron-phonon interactions from first principles. *Rev. Mod. Phys.* **89**, 015003 (2017).
2. Bardeen, J., Cooper, L. N. & Schrieffer, J. R. Theory of superconductivity. *Phys. Rev.* **108**, 1175 (1957).
3. Noffsinger, J. et al. Phonon-assisted optical absorption in silicon from first principles. *Phys. Rev. Lett.* **108**, 167402 (2012).
4. Menéndez, J., Lockwood, D. J., Zwinkels, J. C. & Noël, M. Phonon-assisted optical absorption in germanium. *Phys. Rev. B* **98**, 165207 (2018).
5. Lian, C., Zhang, S., Hu, S., Guan, M. & Meng, S. Ultrafast charge ordering by self-amplified exciton–phonon dynamics in $TiSe_2$. *Nat. Commun.* **11**, 43 (2020).
6. Sayers, C. J. et al. Coherent phonons and the interplay between charge density wave and Mott phases in 1T-$TaSe_2$. *Phys. Rev. B* **102**, 161105(R) (2020).
7. Allen, P. B. Theory of thermal relaxation of electrons in metals. *Phys. Rev. Lett.* **59**, 1460–1463 (1987).
8. Viljas, J. K. & Heikkilä, T. T. Electron-phonon heat transfer in monolayer and bilayer graphene. *Phys. Rev. B* **81**, 245404 (2010).
9. Tse, W.-K. & Das Sarma, S. Energy relaxation of hot Dirac fermions in graphene. *Phys. Rev. B* **79**, 235406 (2009).
10. Freitag, M. S. M. et al. Energy dissipation in graphene field-effect transistors. *Nano Lett.* **9**, 1883–1888 (2009).
11. Park, C. H. et al. Electron–phonon interactions and the intrinsic electrical resistivity of graphene. *Nano Lett.* **14**, 1113–1119 (2014).
12. Kim, T. Y., Park, C. H. & Marzari, N. The electronic thermal conductivity of graphene. *Nano Lett.* **16**, 2439–2443 (2016).
13. Lee, M. M. et al. Efficient hybrid solar cells based on meso-superstructured organometal halide perovskites. *Science* **338**, 643–647 (2012).
14. Yang, W. S. et al. High-performance photovoltaic perovskite layers fabricated through intramolecular exchange. *Science* **348**, 1234–1237 (2015).
15. Park, B. W. et al. Understanding how excess lead iodide precursor improves halide perovskite solar cell performance. *Nat. Commun.* **9**, 3301 (2018).
16. Snaith, H. J. Present status and future prospects of perovskite photovoltaics. *Nat. Mater.* **17**, 372–376 (2018).
17. Pomarico, E. et al. Enhanced electron-phonon coupling in graphene with periodically distorted lattice. *Phys. Rev. B* **95**, 024304 (2017).
18. Sentef, M. A. Light-enhanced electron-phonon coupling from nonlinear electron-phonon coupling. *Phys. Rev. B* **95**, 205111 (2017).
19. Pashkin, A. et al. Femtosecond response of quasiparticles and phonons in superconducting $YBa_2Cu_3O_{7-\delta}$ studied by wideband terahertz spectroscopy. *Phys. Rev. Lett.* **105**, 067001 (2010).
20. Liu, B. et al. Pump frequency resonances for light-induced incipient superconductivity in $YBa_2Cu_3O_{6.5}$. *Phys. Rev. X* **10**, 011053 (2020).
21. Fausti, D. et al. Light-induced superconductivity in a stripe-ordered cuprate. *Science* **331**, 189–191 (2011).
22. Mitrano, M. et al. Possible light-induced superconductivity in K_3C_{60} at high temperature. *Nature* **530**, 461–464 (2016).
23. Buzzi, M. et al. Photomolecular high-temperature superconductivity. *Phys. Rev. X* **10**, 031028 (2020).
24. Knap, M. et al. Dynamical cooper pairing in nonequilibrium electron-phonon systems. *Phys. Rev. B* **94**, 214504 (2016).
25. Hagenmüller, D. et al. Enhancement of the electron–phonon scattering induced by intrinsic surface plasmon–phonon polaritons. *ACS Photonics* **6**, 1073–1081 (2019).
26. Na, M. X. et al. Direct determination of mode-projected electron-phonon coupling in the time domain. *Science* **6**, 1231–1236 (2019).
27. Obergfell, M. & Demsar, J. Tracking the time evolution of the electron distribution function in copper by femtosecond broadband optical spectroscopy. *Phys. Rev. Lett.* **124**, 037401 (2020).
28. Castro Neto, A. H. et al. The electronic properties of graphene. *Rev. Mod. Phys.* **81**, 109 (2009).
29. Wang, F. et al. Gate-variable optical transitions in graphene. *Science* **320**, 206–209 (2008).
30. Kuzmenko, A. B., van Heumen, E., Carbone, F. & van der Marel, D. Universal optical conductance of graphite. *Phys. Rev. Lett.* **100**, 117401 (2008).
31. Nair, R. R. et al. Fine structure constant defines visual transparency of graphene. *Science* **320**, 1308 (2008).

32. Ishioka, K. et al. Ultrafast electron-phonon decoupling in graphite. *Phys. Rev. B* **77**, 121402(R) (2008).
33. Ferrari, A. C. & Basko, D. Raman spectroscopy as a versatile tool for studying the properties of graphene. *Nat. Nanotechnol.* **8**, 235–246 (2013).
34. Sohier, T. et al. Phonon-limited resistivity of graphene by first-principles calculations: electron-phonon interactions, strain-induced gauge field, and Boltzmann equation. *Phys. Rev. B* **90**, 125414 (2014).
35. Ferrari, A. C. Raman spectroscopy of graphene and graphite: disorder, electron–phonon coupling, doping and nonadiabatic effects. *Solid State Commun.* **143**, 47–57 (2007).
36. Pisana, S. et al. Breakdown of the adiabatic Born–Oppenheimer approximation in graphene. *Nat. Mater.* **6**, 198–201 (2007).
37. Wang, Z. et al. Tailoring the nature and strength of electron–phonon interactions in the $SrTiO_3$(001) 2D electron liquid. *Nat. Mater.* **15**, 835–839 (2016).
38. van Mechelen, J. L. et al. Electron-phonon interaction and charge carrier mass enhancement in $SrTiO_3$. *Phys. Rev. Lett.* **100**, 226403 (2008).
39. Gierz, I. et al. Snapshots of non-equilibrium Dirac carrier distributions in graphene. *Nat. Mater.* **12**, 1119–1124 (2013).
40. Winzer, T., Malić, E. & Knorr, A. Microscopic mechanism for transient population inversion and optical gain in graphene. *Phys. Rev. B* **87**, 165413 (2013).
41. Jensen, S. A. et al. Competing ultrafast energy relaxation pathways in photoexcited graphene. *Nano Lett.* **14**, 5839–5845 (2014).
42. Rohde, G. et al. Ultrafast formation of a Fermi-Dirac distributed electron gas. *Phys. Rev. Lett.* **121**, 256401 (2018).
43. Johannsen, J. C. et al. Tunable carrier multiplication and cooling in graphene. *Nano Lett.* **15**, 326–331 (2015).
44. Gierz, I. et al. Tracking primary thermalization events in graphene with photoemission at extreme time scales. *Phys. Rev. Lett.* **115**, 086803 (2015).
45. Brida, D. et al. Ultrafast collinear scattering and carrier multiplication in graphene. *Nat. Commun.* **4**, 1987 (2013).
46. Tielrooij, K. et al. Photoexcitation cascade and multiple hot-carrier generation in graphene. *Nat. Phys.* **9**, 248–253 (2013).
47. Tani, S., Blanchard, F. & Tanaka, K. Ultrafast carrier dynamics in graphene under a high electric field. *Phys. Rev. Lett.* **109**, 166603 (2012).
48. Winnerl, S. et al. Carrier relaxation in epitaxial graphene photoexcited near the Dirac point. *Phys. Rev. Lett.* **107**, 237401 (2011).
49. Johannsen, J. C. et al. Direct view of hot carrier dynamics in graphene. *Phys. Rev. Lett.* **111**, 027403 (2013).
50. Baker, A. M. R., Alexander-Webber, J. A., Altebaeumer, T. & Nicholas, R. J. Energy relaxation for hot Dirac fermions in graphene and breakdown of the quantum Hall effect. *Phys. Rev. B* **85**, 115403 (2012).
51. Stern, M. J. et al. Mapping momentum-dependent electron-phonon coupling and nonequilibrium phonon dynamics with ultrafast electron diffuse scattering. *Phys. Rev. B* **97**, 165416 (2018).
52. Yang, J. A., Parham, S., Dessau, D. & Reznik, D. Novel electron-phonon relaxation pathway in graphite revealed by time-resolved raman scattering and angle-resolved photoemission spectroscopy. *Sci. Rep.* **7**, 40876 (2017).
53. Tang, T. T. et al. A tunable phonon–exciton Fano system in bilayer graphene. *Nat. Nanotechnol.* **5**, 32–36 (2010).
54. Beck, M. et al. Transient increase of the energy gap of superconducting NbN thin films excited by resonant narrow-band terahertz pulses. *Phys. Rev. Lett.* **110**, 267003 (2013).
55. Giovannini, U. D., Hübener, H., Sato, S. A. & Rubio, A. Direct measurement of electron-phonon coupling with time-resolved ARPES. *Phys. Rev. Lett.* **125**, 136401 (2020).
56. Ma, W. et al. Recent progresses in real-time local-basis implementation of time dependent density functional theory for electron–nucleus dynamics. *Comput. Mater. Sci.* **112**, 478–486 (2016).
57. Noda, M. et al. SALMON: Scalable ab-initio light–matter simulator for optics and nanoscience. *Comput. Phys. Commun.* **235**, 356–365 (2019).
58. Pemmaraju, C. D. et al. Velocity-gauge real-time TDDFT within a numerical atomic orbital basis set. *Comput. Phys. Commun.* **226**, 30–38 (2018).
59. Tancogne-Dejean, N., Mucke, O. D., Kartner, F. X. & Rubio, A. Impact of the electronic band structure in high-harmonic generation spectra of solids. *Phys. Rev. Lett.* **118**, 087403 (2017).
60. Bretschneider, S. et al. Quantifying polaron formation and charge carrier cooling in lead-iodide perovskites. *Adv. Mater.* **30**, 1707312 (2018).
61. Suo, P. et al. Observation of negative terahertz photoconductivity in large area type-II Dirac semimetal $PtTe_2$. *Phys. Rev. Lett.* **126**, 227402 (2021).
62. Sinner, A. & Ziegler, K. Quantum Hall effect induced by electron–phonon interaction. *Ann. Phys.* **418**, 168199 (2020).
63. Heidari, S., Cortijo, A. & Asgari, R. Hall viscosity for optical phonons. *Phys. Rev. B* **100**, 165427 (2019).
64. Heidari, S. & Asgari, R. Chiral Hall effect in strained Weyl semimetals. *Phys. Rev. B* **101**, 165309 (2020).
65. Kampfrath, T. et al. Strongly coupled optical phonons in the ultrafast dynamics of the electronic energy and current relaxation in graphite. *Phys. Rev. Lett.* **95**, 187403 (2005).
66. Kuzmenko, A. B. et al. Gate tunable infrared phonon anomalies in bilayer graphene. *Phys. Rev. Lett.* **103**, 116804 (2009).
67. Li, Z. et al. Structure-dependent Fano resonances in the infrared spectra of phonons in few-layer graphene. *Phys. Rev. Lett.* **108**, 156801 (2012).
68. Coulter, J. et al. Uncovering electron-phonon scattering and phonon dynamics in type-I Weyl semimetals. *Phys. Rev. B* **100**, 220301(R) (2019).
69. Zhang, K. et al. Anisotropic Fano resonance in the Weyl semimetal candidate LaAlSi. *Phys. Rev. B* **102**, 235162 (2020).
70. Bonini, N., Lazzeri, M., Marzari, N. & Mauri, F. Phonon anharmonicities in graphite and graphene. *Phys. Rev. Lett.* **99**, 176802 (2007).
71. Yan, H. et al. Time-resolved Raman spectroscopy of optical phonons in graphite: phonon anharmonic coupling and anomalous stiffening. *Phys. Rev. B* **80**, 121403 (R) (2009).
72. Lin, J. et al. Anharmonic phonon effects in Raman spectra of unsupported vertical graphene sheets. *Phys. Rev. B* **83**, 125430 (2011).
73. Lazzeri, M. & Mauri, F. Nonadiabatic Kohn anomaly in a doped graphene monolayer. *Phys. Rev. Lett.* **97**, 266407 (2006).
74. Yan, J., Henriksen, E. A., Kim, P. & Pinczuk, A. Observation of anomalous phonon softening in bilayer graphene. *Phys. Rev. Lett.* **101**, 136804 (2008).
75. Yan, J., Zhang, Y., Kim, P. & Pinczuk, A. Electric field effect tuning of electron-phonon coupling in graphene. *Phys. Rev. Lett.* **98**, 166802 (2007).
76. Castro Neto, A. H. & Guinea, F. Electron-phonon coupling and Raman spectroscopy in graphene. *Phys. Rev. B* **75**, 045404 (2007).
77. Basko, D. M., Piscanec, S. & Ferrari, A. C. Electron-electron interactions and doping dependence of the two-phonon Raman intensity in graphene. *Phys. Rev. B* **80**, 165413 (2009).
78. Malard, L. M., Elias, D. C., Alves, E. S. & Pimenta, M. A. Observation of distinct electron-phonon couplings in gated bilayer graphene. *Phys. Rev. Lett.* **101**, 257401 (2008).
79. Kohn, W. Image of the Fermi surface in the vibration spectrum of a metal. *Phys. Rev. Lett.* **2**, 393–394 (1959).
80. Piscanec, S. et al. Kohn anomalies and electron-phonon interactions in graphite. *Phys. Rev. Lett.* **93**, 185503 (2004).
81. Ando, T. Anomaly of optical phonon in monolayer graphene. *J. Phys. Soc. Jpn.* **75**, 124701 (2006).
82. Froehlicher, G. & Berciaud, S. Raman spectroscopy of electrochemically gated graphene transistors: geometrical capacitance, electron-phonon, electron-electron, and electron-defect scattering. *Phys. Rev. B* **91**, 205413 (2015).
83. Allen, P. B. New method for solving Boltzmann's equation for electrons in metals. *Phys. Rev. B* **17**, 3725 (1978).
84. Grimvall, G. The Electron-Phonon Interaction in Metals (Elsevier, New York, 1981).
85. Calandra, M. & Mauri, F. Electron-phonon coupling and electron self-energy in electron-doped graphene: Calculation of angular-resolved photoemission spectra. *Phys. Rev. B* **76**, 205411 (2007).
86. Ferrante, C. et al. Raman spectroscopy of graphene under ultrafast laser excitation. *Nat. Commun.* **9**, 308 (2018).
87. Kaindl, R. A. et al. Dynamics of Cooper pair formation in $Bi_2Sr_2CaCu_2O_{8+\delta}$. *Phys. Rev. B* **72**, 060510(R) (2005).
88. Smallwood, C. L. et al. Tracking Cooper pairs in a cuprate superconductor by ultrafast angle-resolved photoemission. *Science* **336**, 1137–1139 (2012).
89. Giusti, F. et al. Signatures of enhanced superconducting phase coherence in optimally doped $Bi_2Sr_2Y_{0.08}Ca_{0.92}Cu_2O_{8+\delta}$ driven by midinfrared pulse excitations. *Phys. Rev. Lett.* **122**, 067002 (2019).
90. Papenkort, T., Axt, V. M. & Kuhn, T. Coherent dynamics and pump-probe spectra of BCS superconductors. *Phys. Rev. B* **76**, 224522 (2007).
91. Perfetti, L. et al. Ultrafast dynamics of fluctuations in high-temperature superconductors far from equilibrium. *Phys. Rev. Lett.* **114**, 067003 (2015).
92. Sun, F. et al. Coherent helix vacancy phonon and its ultrafast dynamics waning in topological Dirac semimetal Cd_3As_2. *Phys. Rev. B* **95**, 235108 (2017).
93. Higuchi, T. et al. Light-field-driven currents in graphene. *Nature* **550**, 224–228 (2017).
94. Nguyen, T. et al. Topological singularity induced chiral Kohn anomaly in a Weyl semimetal. *Phys. Rev. Lett.* **124**, 236401 (2020).
95. Lin, Z., Zhigilei, L. V. & Celli, V. Electron-phonon coupling and electron heat capacity of metals under conditions of strong electron-phonon nonequilibrium. *Phys. Rev. B* **77**, 075133 (2008).
96. Bertrand, S., Parent, J.-M., Côté, R. & Garate, I. Complete optical valley polarization in Weyl semimetals in strong magnetic fields. *Phys. Rev. B* **100**, 075107 (2019).
97. Mak, K. F., He, K., Shan, J. & Heinz, T. F. Control of valley polarization in monolayer MoS_2 by optical helicity. *Nat. Nanotechnol.* **7**, 494–498 (2012).
98. Bertrand, S., Garate, I. & Côté, R. Light-induced valley polarization in interacting and nonlinear Weyl semimetals. *Phys. Rev. B* **96**, 075126 (2017).

99. Soler, J. M. et al. The SIESTA method for ab initio order-N materials simulation. *J. Phys. Condens. Matter* **14**, 2745 (2002).
100. Chang, C.-Z. et al. Observation of the quantum anomalous Hall insulator to Anderson insulator quantum phase transition and its scaling behavior. *Phys. Rev. Lett.* **117**, 126802 (2016).
101. Chen, N.-K. et al. Directional forces by momentumless excitation and order-to-order transition in peierls-distorted solids: the case of GeTe. *Phys. Rev. Lett.* **120**, 185701 (2018).
102. Apostolov, A. T., Apostolova, I. N. & Wesselinowa, J. M. Temperature and layer number dependence of the G and 2D phonon energy and damping in graphene. *J. Phys. Condens. Matter* **24**, 235401 (2012).
103. Meng, S. & Kaxiras, E. Real-time, local basis-set implementation of time-dependent density functional theory for excited state dynamics simulations. *J. Chem. Phys.* **129**, 054110 (2008).
104. Lian, C., Hu, S., Guan, M. & Meng, S. Momentum-resolved TDDFT algorithm in atomic basis for real time tracking of electronic excitation. *J. Chem. Phys.* **149**, 154104 (2018).
105. Lian, C., Guan, M., Hu, S., Zhang, J. & Meng, S. Photoexcitation in solids: first principles quantum simulations by real-time TDDFT. *Adv. Theory Simul.* **1**, 1800055 (2018).

ACKNOWLEDGEMENTS

We acknowledge financial support from MOST (grant 2021YFA1400200), NSFC (grants 12025407, 11934003, 91850120, 11774328), and CAS (XDB330301).

AUTHOR CONTRIBUTIONS

S.M. conceived and supervised the project. S.-Q.H., X.-B.L., C.L. and H.Z. performed the theoretical modelling and TDDFT calculations. C.L. contributed to the software code. S.-Q.H., H.Z., X.-B.L., and S.M. analysed the data. The manuscript is written by S.-Q.H. and S.M., with contributions from H.Z., X.-B.L. and M.-X.G. All authors discussed and contributed to the manuscript.

COMPETING INTERESTS

The authors declare no competing interests.

ADDITIONAL INFORMATION

Supplementary information The online version contains supplementary material available at https://doi.org/10.1038/s41535-021-00421-7.

Correspondence and requests for materials should be addressed to Sheng Meng.

Reprints and permission information is available at http://www.nature.com/reprints

Publisher's note Springer Nature remains neutral with regard to jurisdictional claims in published maps and institutional affiliations.